PROCEEDINGS OF SCIENCE

W^+W^- + jet: compact analytic results

John Campbell
Fermilab
E-mail: johnmc@fnal.gov

David Miller
University of Glasgow
E-mail: d.miller@physics.gla.ac.uk

Tania Robens*
IKTP, TU Dresden
E-mail: tania.robens@tu-dresden.de

In the second run of the LHC, which started in April 2015, an accurate understanding of Standard Model processes is more crucial than ever. Processes including electroweak gauge bosons serve as standard candles for SM measurements, and equally constitute important background for BSM searches. We here present the NLO QCD virtual contributions to W^+W^- + jet in an analytic format obtained through unitarity methods and show results for the full process using an implementation into the Monte Carlo event generator MCFM. Phenomenologically, we investigate total as well as differential cross sections for the LHC with 14 TeV center-of-mass energy, as well as a future 100 TeV proton-proton machine. In the format presented here, the one–loop virtual contributions also serve as important ingredients in the calculation of W^+W^- pair production at NNLO.

FERMILAB-CONF-16-006-T

12th International Symposium on Radiative Corrections (Radcor 2015) and LoopFest XIV (Radiative Corrections for the LHC and Future Colliders)
15-19 June, 2015
UCLA Department of Physics & Astronomy Los Angeles, USA

*Speaker.

1. Overview

We here consider the hadronic production of W pairs in association with a single jet at next-to-leading order (NLO) in QCD at a hadron collider with a center-of-mass energy of 14 and 100 TeV, respectively. The W bosons decay leptonically, with all spin correlations included. At tree level this process corresponds to the partonic reaction,

$$\begin{array}{l} q+\bar{q} \to W^+ + W^- + g \\ \qquad\qquad\quad \big| \qquad\quad \big| \to \mu^- + \nu_\mu \\ \qquad\qquad\quad \big| \to \nu_e + e^+ \end{array} \tag{1.1}$$

with all possible crossings of the partons between initial and final states. Tree level diagrams for this process are shown in Fig. 1.

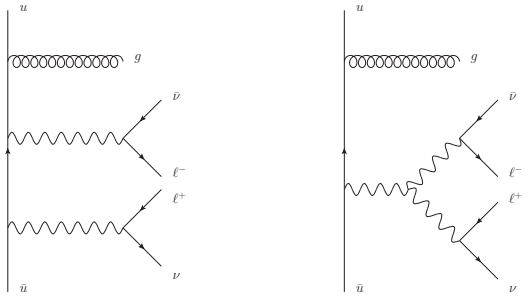

(a) (b)

Figure 1: Sample diagrams entering the calculation of the leading order amplitude for the WW+jet process, corresponding to (a) W emission from the quark line and (b) emission from an intermediate Z boson or photon.

At next-to-leading order we must include the emission of an additional parton, either as a virtual particle to form a loop amplitude, or as a real external particle. Sample diagrams for virtual NLO contributions are shown in Fig. 2; in addition, one-loop corrections to Fig. 1 (b) must be included. All results presented in the following have been obtained using the calculation of Ref. [1], where virtual corrections have been obtained using generalized unitarity methods [2, 3, 4, 5, 6, 7] as follows: Each amplitude is decomposed in terms of the usual one-loop basis

$$\mathscr{A}(\{p_i\}) = \sum_j d_j I_4^j + \sum_j c_j I_3^j + \sum_j b_j I_2^j + R\,. \tag{1.2}$$

In this equation I_n^j represents a scalar loop integral with n propagators, commonly referred to as box ($n=4$), triangle ($n=3$) and bubble ($n=2$) integrals. The integral coefficients d_j, c_j and b_j can be obtained by the application of unitarity cuts in four dimensions. The rational remainder term R can be determined using similar cutting rules, after the inclusion of a fictitious mass for the particles propagating in the loop. Since the tree-level on-shell amplitudes that appear in the cutting procedure are quite complex, this procedure has been performed with the help of the S@M

Mathematica package [8]. The evaluation of the scalar integrals appearing in Eq. (1.2) has been performed using the QCDLoop Fortran library [9].

The combination of the virtual contributions with born and real emission diagrams has been implemented using MCFM [10, 11]. Note that we do not include the effects of any third-generation quarks, either as external particles or in internal loops.

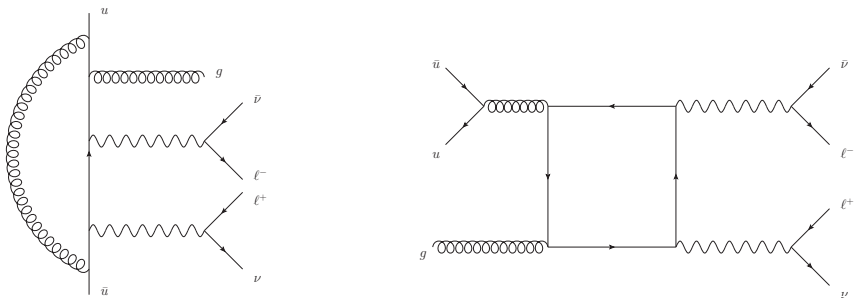

Figure 2: Sample diagrams entering the calculation of the one-loop amplitude for the WW+jet process. The one-loop diagrams can be categorized according to whether a gluon dresses a leading-order amplitude (left), or whether the diagram includes a closed fermion loop (right).

2. Coefficients

We consider all particles outgoing and consider the process,

$$0 \to q^-(p_1) + \bar{q}^+(p_2) + \ell^-(p_3) + \bar{\ell}^+(p_4) + \ell^-(p_5) + \bar{\ell}^+(p_6) + g^+(p_7)\,, \tag{2.1}$$

Tree-level amplitudes for this process have been presented in detail in Refs. [12, 13], whose notation we follow closely.

As a representative box integral coefficient we choose the one corresponding to the basis integral $I_4\left(s_{56}, s_{34}, 0, s_{17}; s_{127}, s_{234}\right)$. We here show the leading color integral coefficient, which receives a pre-factor of N_c. It can be written as,

$$\begin{aligned} d\left(s_{56}, s_{34}, 0, s_{17}; s_{127}, s_{234}\right) = & \frac{1}{s_{34} - m_W^2} \frac{1}{s_{56} - m_W^2} \frac{\langle 12\rangle^2 \langle 2|P|2]}{2\langle 27\rangle \langle 17\rangle} \times \\ & \left([42] - \frac{\langle 2|P|4]}{D}\right) \left(\langle 3|2+4|6] - \frac{\langle 23\rangle \langle 2|P|6]}{D}\right) \left(\frac{[71]\langle 15\rangle}{\langle 2|P|7]} + \frac{\langle 25\rangle}{D}\right) \end{aligned} \tag{2.2}$$

where the compound momentum P and denominator factor D are defined by,

$$P = s_{17}\, p_{34} + s_{234} p_{17}, \qquad D = \langle 2|(3+4)\,(1+7)|2\rangle. \tag{2.3}$$

The factors of D can be put into a more familiar form by relating them to the product $DD^\star$, where the complex conjugate of D is simply given by $D^\star = [2|(3+4)\,(1+7)|2]$. The product can be written as a trace of gamma matrices that evaluates to,

$$DD^\star = 4 s_{34} (p_2 \cdot p_{17})^2 + 4 s_{17} (p_2 \cdot p_{34})^2 - 8 (p_2 \cdot p_{17})(p_2 \cdot p_{34})(p_{17} \cdot p_{34})\,. \tag{2.4}$$

m_W	80.385 GeV	Γ_W	2.085 GeV
m_Z	91.1876 GeV	Γ_Z	2.4952 GeV
e^2	0.095032	g_W^2	0.42635
$\sin^2\theta_W$	0.22290	G_F	0.116638×10^{-4}

Table 1: The values of the mass, width and electroweak parameters used to produce the results in this paper.

This is just the Gram determinant for this basis integral; its presence, when raised to a sufficiently high power, can lead to numerical instability in phase space regions where it is very small. To avoid any such issues we veto phase regions where cancellations between the terms in Eq. (2.4) (and equivalent expressions for the other box integrals) occur at the level of 10^{-6} or more. In our studies this occurs only very rarely, in about one in a million events, so that the effects of such a veto are tiny compared to the anticipated level of precision.

3. Total cross sections

The results presented in this section have been obtained using the parameters shown in Table 1. In calculations of LO quantities we employ the CTEQ6L1 PDF set [14], while at NLO we use CT10 [15]. The renormalization and factorization scales are usually chosen to be the same, $\mu_R = \mu_F = \mu$, with our default scale choice $\mu = \mu_0$ given by,

$$\mu_0 \equiv \frac{H_T}{2} = \frac{1}{2}\sum_i p_\perp^i \, . \tag{3.1}$$

The sum over the index i runs over all final state leptons and partons. Jets are defined using the anti-k_T algorithm with separation parameter $R = 0.5$ and must satisfy,

$$p_\perp^{\rm jet} > p_{\perp,\rm cut}^{\rm jet} \, , \qquad |\eta^{\rm jet}| < 4.5 \, . \tag{3.2}$$

The cross-sections predicted at LO and NLO are shown in Fig. 3, as a function of $p_{\perp,\rm cut}^{\rm jet}$ and for values as large as 400 GeV at the 100 TeV machine. The theoretical uncertainty band is computed by using a series of scale variations about the central choice μ_0. The uncertainty corresponds to scale variations of $\{\mu_R,\mu_F\} = \{2\mu_0, 2\mu_0\}, \{\mu_0/2, \mu_0/2\}$ for 14 TeV and $\{\mu_R,\mu_F\} = \{2\mu_0, \mu_0/2\}, \{\mu_0/2, 2\mu_0\}$ for 100 TeV. The cross-sections at NLO are significantly larger than those at LO and, in general, the uncertainty bands do not overlap. At 100 TeV the cross-sections are about an order of magnitude larger than at 14 TeV.

As useful operating points, we use $p_{\perp,\rm cut}^{\rm jet} = 25$ GeV at both collider energies and also choose to study the additional case $p_{\perp,\rm cut}^{\rm jet} = 300$ GeV at 100 TeV, which we will label 100 TeV* in the following. The cross-sections for WW+jet production at these colliders, under the basic jet cuts of Eq. (3.2), are collated in Table 2 [1]. Note that the effect of the decays of the W bosons is not included. At the 100 TeV machine, the jet cut of 300 GeV has been chosen so that the cross section

[1] Note that there is a minor typographical error in Ref. [1] in the relative uncertainty due to scale variations for the LO cross section at 100 TeV, which we have corrected here.

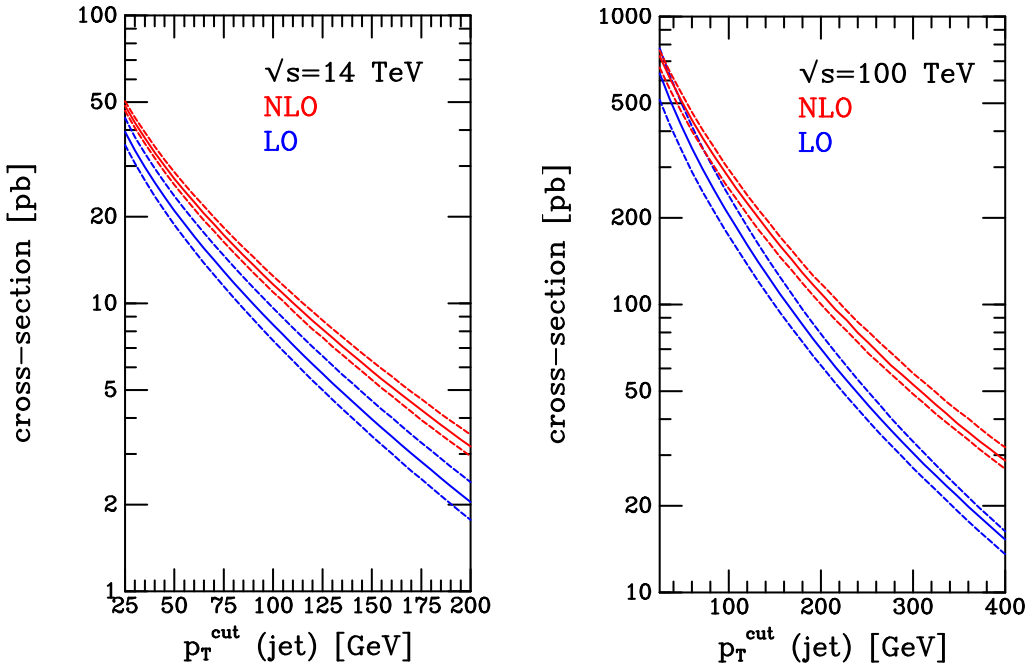

Figure 3: Cross-sections at $\sqrt{s} = 14$ TeV (left) and 100 TeV (right), as a function of the transverse momentum cut on the jet. The prediction at each order is shown as a solid line, with the dotted lines indicating the scale uncertainty corresponding to a factor of two variation about the central scale.

$\sqrt{s}$	$p_{\perp,\mathrm{cut}}^{\mathrm{jet}}$	σ_{LO} [pb]	σ_{NLO} [pb]
14 TeV	25 GeV	$39.5^{+11.7\%}_{-11.0\%}$	$48.6^{+3.8\%}_{-4.0\%}$
100 TeV	25 GeV	$648^{+22.3\%}_{-19.3\%}$	$740^{+4.5\%}_{-9.3\%}$
100 TeV	300 GeV	$30.3^{+11.22\%}_{-10.56\%}$	$53.7^{+8.0\%}_{-7.6\%}$

Table 2: Cross-sections for the process $pp \to WW$+jet at proton-proton colliders of various energies, together with estimates of the theoretical uncertainty from scale variation as described in the text. Monte Carlo uncertainties are at most a single unit in the last digit shown shown in the table.

is similar in size to the 14 TeV cross section, as can be seen from Table 2. This cut provides a useful benchmark in a different kinematic regime that may be more appropriate at that collider energy.

An interesting feature of the higher order corrections to processes such as the one at hand is the existence of so-called "giant K-factors" [16]. These are due to the existence of kinematic configurations at NLO that do not exist at LO and that can be the dominant contribution in certain distributions. An observable that exemplifies this effect is H_T^{jets}, which is defined to be the scalar sum of all jet transverse momenta in a given event. At NLO, real radiation contributions arise in which two hard partons are produced approximately back-to-back, with the W^+W^- system relatively soft. Such configurations are not captured at all by the LO calculations, in which the parton and W^+W^- system are necessarily balanced in the transverse plane. This results in the by now well-known feature of huge NLO corrections at large H_T^{jets}, as shown in Fig. 4. Similar effects are

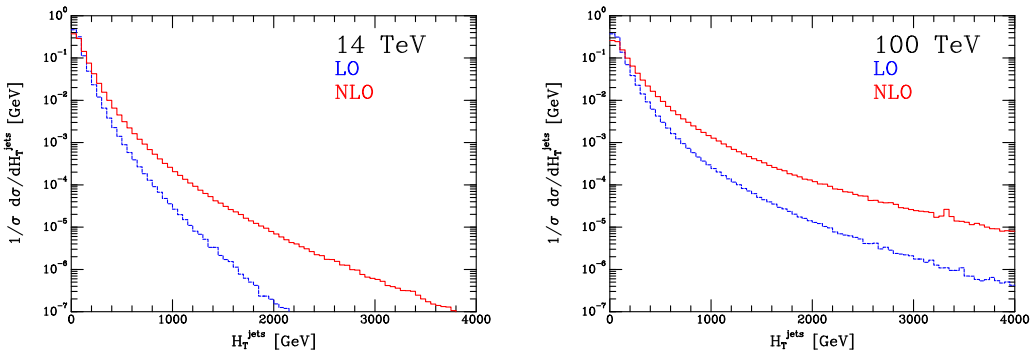

Figure 4: The distribution of the observable $H_T^{\text{jets}} = \sum_{\text{jets}} p_\perp^{\text{jet}}$ at LO and NLO, for 14 TeV (left) and 100 TeV (right).

variable	cut
$p_{\perp,j}$	> 25 GeV
$\lvert\eta_j\rvert$	< 4.5
$\lvert\eta_\ell\rvert$	< 2.5
$p_{\perp,\ell_1}$	> 22 GeV
$p_{\perp,\ell_2}$	> 15 GeV
$m_{\ell\ell}$	$\in [10,80]$ GeV
$p_\perp^{\text{miss}}$	> 20 GeV
$\Delta\Phi_{\ell\ell}$	< 2.8
$m_T^{\ell\ell}$	< 150 GeV
$\max[m_T^{\ell_1}, m_T^{\ell_2}]$	> 50 GeV

Table 3: Cuts applied in the 14 TeV analysis, corresponding to the "full" set of cuts. The jet cuts, corresponding to the first two lines in the table, are the only ones applied for the "basic" cross-section.

observed at both energies, with NLO predictions at least an order of magnitude larger than their LO counterparts in the tails of the distributions. At 100 TeV the onset of the giant K-factor is a little slower, but still occurs well before the interesting multi-TeV region.

4. Differential distributions

We first consider the case of 14 TeV LHC running, with a set of cuts inspired by the ATLAS determination of the spin and parity of the Higgs boson presented in Ref. [17]. The WW process constitutes the largest irreducible background in the $H \to WW^\star$ decay channel and a cocktail of cuts must be applied in order to access information about the Higgs boson. The cuts are summarized in Table 3. These include constraints on the transverse mass of (X, E_T^{miss}) systems, m_T^X, where $X \in (\ell\ell, \ell_1, \ell_2)$, with $p_{\ell\ell} = p_{\ell_1} + p_{\ell_2}$. This quantity is defined by[2],

$$m_T^X = \sqrt{2\, p_\perp^X E_T^{\text{miss}} \left(1 - \cos\Delta\Phi(\overrightarrow{p}_T^X, \overrightarrow{E}_T^{\text{miss}})\right)}. \tag{4.1}$$

[2] See, for instance, Eq. (3) of Ref. [18].

cuts	$\sigma^{\rm LO}$ [fb]	$\sigma^{\rm NLO}$ [fb]	K
basic	462.0(2)	568.4(2)	1.23
full	67.12(4)	83.91(5)	1.25

Table 4: Cross-sections at 14 TeV. Monte Carlo uncertainties are indicated in parentheses and are smaller than the per mille level.

In the results that follow we shall always consider the decay of each W boson into a single lepton family, i.e. the Born level quark-antiquark process we consider is the one shown in Eq. (1.1). The cross-sections under these cuts are given in Table 4. In order to assess their effect, we also show for comparison the cross sections obtained using only the jet cuts, i.e. the top two lines of the cuts in Table 3. The table also shows the K-factor, defined by $K = \sigma^{\rm NLO}/\sigma^{\rm LO}$, which we find is rather insensitive to which set of cuts is applied.

We now consider differential distributions in $m_T^{\ell\ell}$, $\Delta\Phi_{\ell\ell}$ and $m_{\ell\ell}$ as well as the transverse momentum of the lead jet, $p_\perp^{j_1}$. These quantities are shown in Figure 5 where, for comparison, the LO prediction has been rescaled by the K-factor from Table 4. This indicates that there is very little difference between the shapes of the distributions at each order, with the exception of the transverse momentum of the leading jet. In contrast this does receive significant corrections, which is expected since additional radiation beyond a single jet is only present at NLO.

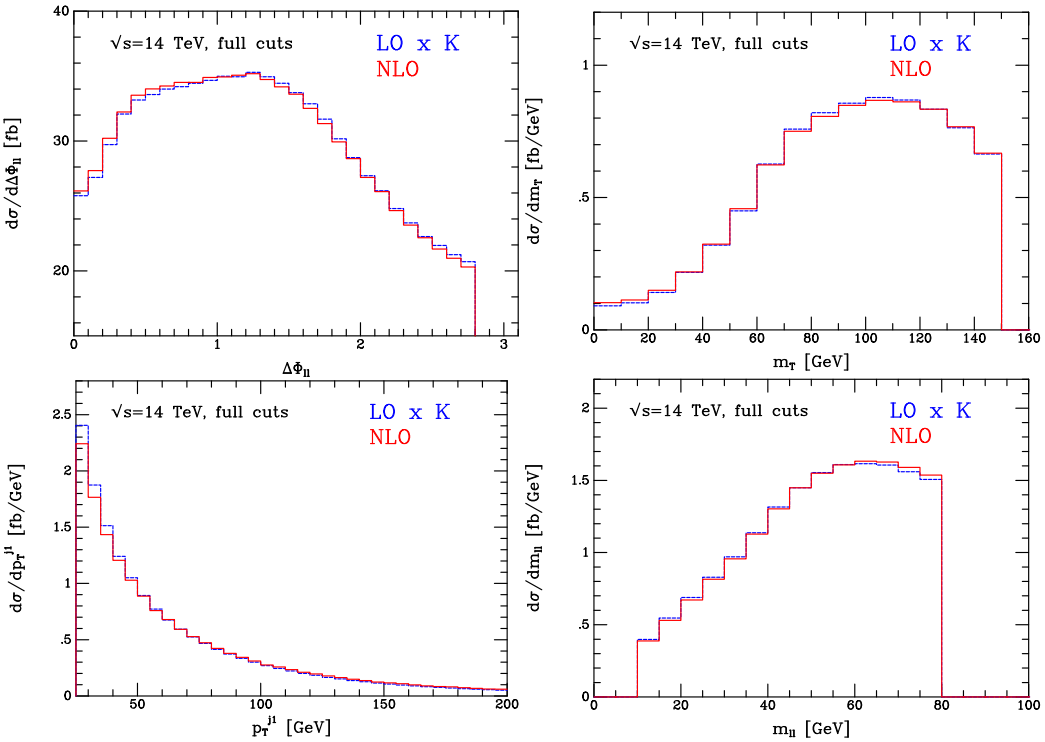

Figure 5: Kinematic distributions at 14 TeV, using the full set of cuts specified in the text. The NLO prediction is shown as the solid (red) histogram, while the dashed (blue) histogram corresponds to the LO prediction rescaled by the K-factor.

To illustrate some of the key differences between the predictions for WW+jet production at 14 and 100 TeV, we now examine NLO predictions for a number of kinematic distributions and

compare their behaviour at different c.o.m energies. Fig. 6 shows two quantities that characterize the overall nature of this process, the transverse momentum of the leading jet and the scalar sum of all jet and lepton transverse momenta, H_T (c.f. H_T^{jets} earlier). All histograms have been normalized to the total NLO cross-sections given earlier, in order to better compare their shapes. At 100 TeV the leading jet is significantly harder than at 14 TeV. The H_T distribution is also harder at 100 TeV with, of course, a significant shift in the peak once the jet cut is raised. [3]

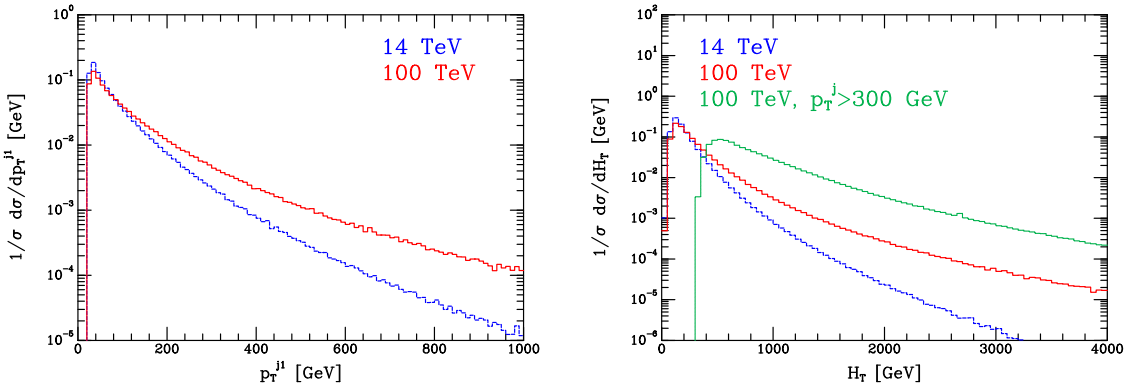

Figure 6: NLO $p_{\perp,j}$ (left) and H_T (right) distributions, normalized by the respective total cross sections, for 14 TeV(red), 100 TeV(blue), and 100 TeV* (green)

Turning to leptonic observables, Fig. 7 shows the transverse momentum and rapidity of the positron from the W^+ decay. The transverse momentum spectrum of the positron falls much less steeply at 100 TeV, and even less so with a higher jet cut. The rapidity distribution of the positron is also changed non-trivially, with the broader peak at 100 TeV reflecting the fact that the process is probing a much smaller parton fraction. When the jet cut is raised to 300 GeV the required parton fraction is again larger so that the shape is a little closer to the one found at 14 TeV. [4] An observable

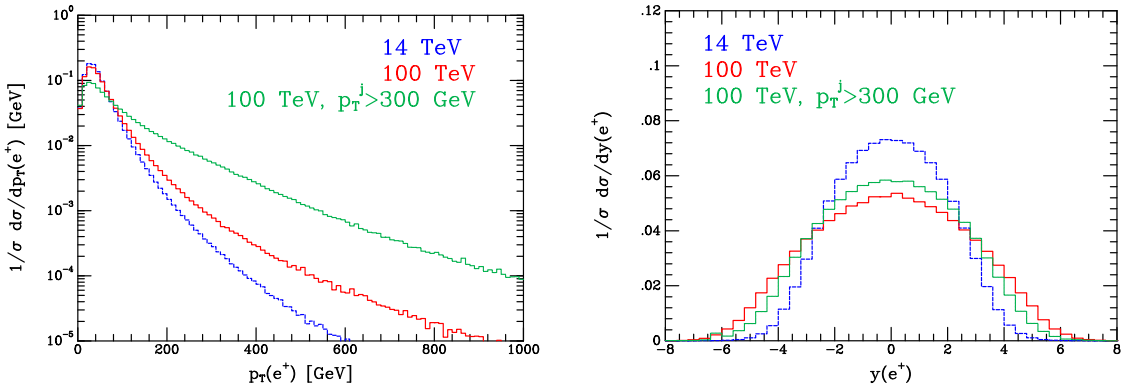

Figure 7: NLO $p_{\perp,\ell}$ (left) and η_ℓ (right) distributions, normalized by the respective total cross sections, for 14 TeV(red), 100 TeV(blue), and 100 TeV* (green)

that is particularly interesting for this process is the azimuthal angle between the electron and the

[3] This variable is also frequently used as a cut variable in searches for physics beyond the SM, for example in Refs. [19, 20], where cuts are placed in the range $\sim$ 0.6–2 TeV depending on the details of the search strategy.

[4] Although not shown here, the jet rapidity exhibits a similar behaviour.

positron, which can be used to isolate contributions to this final state from Higgs boson decays. As shown in Fig. 8, under the usual jet cuts at 14 TeV, this distribution is peaked towards $\Delta\Phi_{\ell\ell} = \pi$, a feature which persists at 100 TeV using the same jet cut. Once the jet cut is raised significantly, the recoil of the W^+W^- system results in the two leptons instead being preferentially produced closer together, i.e. in the region $\Delta\Phi_{\ell\ell} \to 0$. This is the same region of $\Delta\Phi_{\ell\ell}$ that is favoured by events produced via the Higgs boson decay. Even if the jet threshold at a 100 TeV collider were not as high as 300 GeV, such a shift in this distribution could be an important consideration in optimizing Higgs-related analyses in the W^+W^- decay channel. Despite this shift to smaller $\Delta\Phi_{\ell\ell}$,

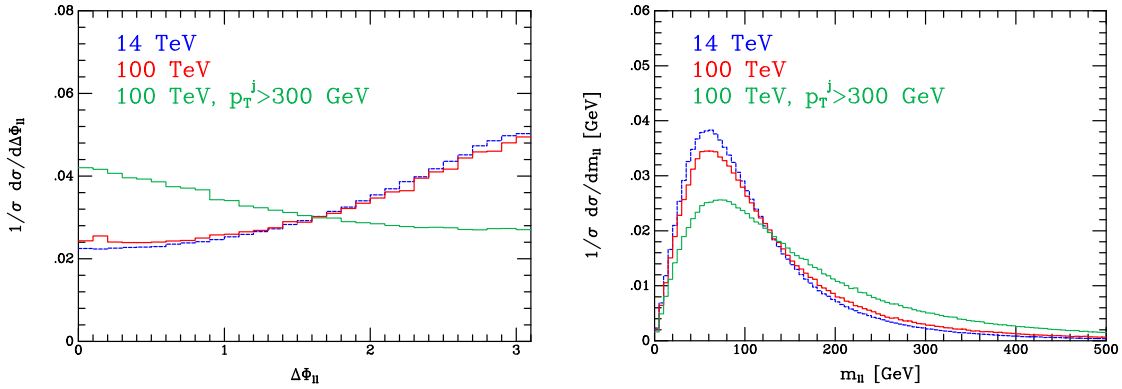

Figure 8: NLO $\Delta\Phi_{\ell\ell}$ (left) and $m_{\ell\ell}$ (right) distributions, normalized by the respective total cross sections, for 14 TeV(red), 100 TeV(blue), and 100 TeV* (green)

the combination of this effect with the change in the $p_{\perp,\ell}$ distribution shown earlier results in a relatively similar distribution for $m_{\ell\ell}$, albeit with a longer tail.

5. Summary

In this contribution we have considered the process W^+W^- + jet at NLO QCD, making use of an analytic calculation implemented into the Monte Carlo event generator MCFM. We have considered total cross sections as well as several differential distributions at proton-proton colliders with 14 TeV and 100 TeV center-of-mass energies. For the latter case we have also considered the effect of increasing the minimum $p_{\perp,j}$ cut by roughly an order of magnitude. We found that in general at 100 TeV dimensionful variables such as $p_\perp$ or $m_{\ell\ell}$ exhibit longer tails in the distributions, reflecting the increased center-of-mass energy of the system; the increase of the center-of-mass energy also leads to broader rapidity distributions. Furthermore, applying a higher $p_\perp$ cut significantly changes distributions for the dilepton azimuthal angle $\Delta\Phi_{\ell\ell}$ as well as the total transverse momentum of the visible system H_T, which are frequently used for background suppression for Higgs measurements or BSM searches, respectively. In case such an increased cut is applied, this needs to be taken into account when devising the respective search strategies at a 100 TeV machine.

Acknowledgements

T.R. would like to thank the Fermilab Theory Group for their repeated hospitality while this work was completed. DJM is supported by the UK Science and Technology Facilities Council

(STFC) under grant ST/L000446/1. This research is supported by the US DOE under contract DE-AC02-07CH11359.

References

[1] John M. Campbell, David J. Miller, and Tania Robens. Next-to-Leading Order Predictions for WW+Jet Production. *Phys. Rev.*, D92(1):014033, 2015, 1506.04801.

[2] Ruth Britto, Freddy Cachazo, and Bo Feng. Generalized unitarity and one-loop amplitudes in N=4 super-Yang-Mills. *Nucl.Phys.*, B725:275–305, 2005, hep-th/0412103.

[3] Ruth Britto, Evgeny Buchbinder, Freddy Cachazo, and Bo Feng. One-loop amplitudes of gluons in SQCD. *Phys.Rev.*, D72:065012, 2005, hep-ph/0503132.

[4] Ruth Britto, Bo Feng, and Pierpaolo Mastrolia. The Cut-constructible part of QCD amplitudes. *Phys.Rev.*, D73:105004, 2006, hep-ph/0602178.

[5] Darren Forde. Direct extraction of one-loop integral coefficients. *Phys.Rev.*, D75:125019, 2007, 0704.1835.

[6] Pierpaolo Mastrolia. Double-Cut of Scattering Amplitudes and Stokes' Theorem. *Phys.Lett.*, B678:246–249, 2009, 0905.2909.

[7] S.D. Badger. Direct Extraction Of One Loop Rational Terms. *JHEP*, 0901:049, 2009, 0806.4600.

[8] D. Maitre and P. Mastrolia. S@M, a Mathematica Implementation of the Spinor-Helicity Formalism. *Comput.Phys.Commun.*, 179:501–574, 2008, 0710.5559.

[9] R. Keith Ellis and Giulia Zanderighi. Scalar one-loop integrals for QCD. *JHEP*, 0802:002, 2008, 0712.1851.

[10] John M. Campbell and R. Keith Ellis. An Update on vector boson pair production at hadron colliders. *Phys.Rev.*, D60:113006, 1999, hep-ph/9905386.

[11] John M. Campbell, R. Keith Ellis, and Walter T. Giele. A Multi-Threaded Version of MCFM. *Eur.Phys.J.*, C75(6):246, 2015, 1503.06182.

[12] Lance J. Dixon, Z. Kunszt, and A. Signer. Helicity amplitudes for O(alpha-s) production of W^+W^-, $W^\pm Z$, ZZ, $W^\pm\gamma$, or $Z\gamma$ pairs at hadron colliders. *Nucl.Phys.*, B531:3–23, 1998, hep-ph/9803250.

[13] John M. Campbell, R. Keith Ellis, and Giulia Zanderighi. Next-to-leading order predictions for $WW+1$ jet distributions at the LHC. *JHEP*, 0712:056, 2007, 0710.1832.

[14] J. Pumplin, D.R. Stump, J. Huston, H.L. Lai, Pavel M. Nadolsky, et al. New generation of parton distributions with uncertainties from global QCD analysis. *JHEP*, 0207:012, 2002, hep-ph/0201195.

[15] Hung-Liang Lai, Marco Guzzi, Joey Huston, Zhao Li, Pavel M. Nadolsky, et al. New parton distributions for collider physics. *Phys.Rev.*, D82:074024, 2010, 1007.2241.

[16] Mathieu Rubin, Gavin P. Salam, and Sebastian Sapeta. Giant QCD K-factors beyond NLO. *JHEP*, 09:084, 2010, 1006.2144.

[17] Georges Aad et al. Determination of spin and parity of the Higgs boson in the $WW^* \to e\nu\mu\nu$ decay channel with the ATLAS detector. *Eur.Phys.J.*, C75(5):231, 2015, 1503.03643.

[18] Vardan Khachatryan et al. Search for a Higgs Boson in the Mass Range from 145 to 1000 GeV Decaying to a Pair of W or Z Bosons. *JHEP*, 10:144, 2015, 1504.00936.

[19] Georges Aad et al. Search for microscopic black holes and string balls in final states with leptons and jets with the ATLAS detector at sqrt(s) = 8 TeV. *JHEP*, 08:103, 2014, 1405.4254.

[20] Georges Aad et al. Search for supersymmetry in events containing a same-flavour opposite-sign dilepton pair, jets, and large missing transverse momentum in $\sqrt{s} = 8$ TeV pp collisions with the ATLAS detector. *Eur. Phys. J.*, C75(7):318, 2015, 1503.03290.